Dalton Transactions

Accepted Manuscript

ROYAL SOCIETY OF CHEMISTRY

www.rsc.org/dalton

Journal Name

RSCPublishing

ARTICLE

Lead-Free Antiferroelectric: xCaZrO$_3$-(1-x)NaNbO$_3$ System ($0 \leq x \leq 0.10$)

Cite this: DOI: 10.1039/xoxxoooooox

Hiroyuki Shimizu[a], Hanzheng Guo[b], Sebastian E. Reyes-Lillo[c], Youichi Mizuno[a], Karin M. Rabe[c] and Clive A. Randall[b]

Received ooth January 2012,
Accepted ooth January 2012

DOI: 10.1039/xoxxoooooox

www.rsc.org/

This study demonstrates that antiferroelectricity can be stabilized in NaNbO$_3$ (NN) based ceramics by lowering the tolerance factor. Through consideration of the crystal chemistry via the Goldschmidt tolerance factor and polarizability, we show that simultaneous substitution of Zr^{4+} and Ca^{2+} ions in the Nb and Na sites, respectively, lowers the polarizability and tolerance factor of the $(Na_{1-x}Ca_x)(Nb_{1-x}Zr_x)O_3$ (CZNN100x) solid solution, while maintaining charge neutrality. Structural investigations using both X-ray diffraction and transmission electron microscopy (TEM) indicated an enhancement of antiferroelectric (AFE) superlattice peaks with CaZrO$_3$ substitution. The TEM domain analysis revealed that only AFE domains existed in the CZNN4 and CZNN5 ceramics; in contrast, normal NN ceramics displayed coexistence of AFE and ferroelectric (FE) domains at room temperature. The CZNN100x ($0.02 \leq x \leq 0.05$) ceramics showed double polarization hysteresis loops, characteristic of reversible AFE ↔ FE phase transition switching. The field-induced polarization decreased drastically with increasing substitution, an effect of the decreases in tolerance factor. In addition, the AFE switching field was increased by the chemical substitution. First principles calculations are performed to obtain insights into the relative stability and coexistence of the AFE and FE phases in single domains. The large decrease of polarization in the CZNN system is explained by a modification of the relative stability of the relevant structures, which favours nonpolar-to-polar AFE transitions over polar-to-polar FE domain switching.

1. Introduction

Antiferroelectric (AFE) materials are characterized by double polarization - electric field (*P*-*E*) hysteresis loops, high electrostatic electrical energy-storage densities compared to ferroelectrics (FEs) and high-permittivity linear dielectrics [1]. In particular, AFE dielectrics are attractive materials for capacitors because the dielectric constant increases as the applied electric field reaches the switching field (E_F), which is the opposite behaviour compared to FE materials where the dielectric constant decreases with increasing applied electric field; this effect is often explained as the voltage - saturation - behaviour. AFE materials also have low dielectric losses, given that there are no extrinsic domain contributions with AFE domain switching. This is an attractive dielectric feature when operating under electrical bias and high ac ripple currents, which is becoming an important requirement for capacitors in power electronic applications.

Well known lead-containing AFE representatives, such as PbZrO$_3$ (PZ), La doped Pb($Zr_{0.95}$,$Ti_{0.05}$)O$_3$ (PLZT), PbHfO$_3$, and Pb($In_{1/2}Nb_{1/2}$)O$_3$ (PIN), show double *P*-*E* loops with reversible AFE ↔ FE phase transitions [2-8]. Most lead-containing AFE ceramics correspond to PZ based chemical modifications, where the addition of Sn, Ti, and Nb, or La optimizes the AFE properties of PZ [3,7-13]. These PZ-based AFEs are of technological importance due to their multiple applications in micro-electromechanical systems and energy-storage devices [14,15]. Similarly, motivated by the recent interest in lead-free piezoelectric ceramics [16,17], research on lead-free AFE materials has focused on ($Bi_{1/2}Na_{1/2}$)TiO$_3$, NaNbO$_3$ (NN), and AgNbO$_3$ [18]. However, these AFE materials are quite different from the lead-containing AFE materials mentioned above. In the case of NN ceramics, the room temperature AFE phase (*P*) has a well-known *Pbma* structure [19,20]. In contrast to the lead-containing AFE ceramics, the NN ceramics do not show double *P*-*E* loops. Instead, square *P*-*E* loops are manifested due to a field-induced metastable FE phase (*Q*) with $P2_1ma$ structure [21-26]. Several researches have previously investigated the *P*/*Q* phases in terms of the complicated features of *P*-*E* hysteresis loops [27,28]. Recently, Mishra *et al.* proposed the existence of competing AFE and FE interactions in NN and reported a coexistence of these two phases over a wide range of temperatures, from 12 to 280 K [29]. Fu *et al.* reported that in the (1-x)AgNbO$_3$-xNN solid solution, the polarization evolves from an uncompensated AFE ordering in AgNbO$_3$ to the FE ordering observed in NN [28]. More recently, Xu *et al.* reported electrical measurements in NN-based lead-free polycrystalline ceramics. The AFE phase of $[(Ag_{0.05}Na_{0.95})_{1-x}K_x]NbO_3$ ceramics can be driven to AFE - FE phase boundary at x = 2.3%, where a kinetic competition between AFE phase transitions and FE domain reversal was observed [27]. In the same work, it was pointed out that the rather slow kinetics of AFE back switching can be suppressed

with high frequency ac fields, effectively inducing an AFE back switching from the FE phase with decreasing applied external field. All these studies highlight a major limitation of the critical back switching behavior in NN based ceramics, due to the relative stability of the FE and AFE structures.

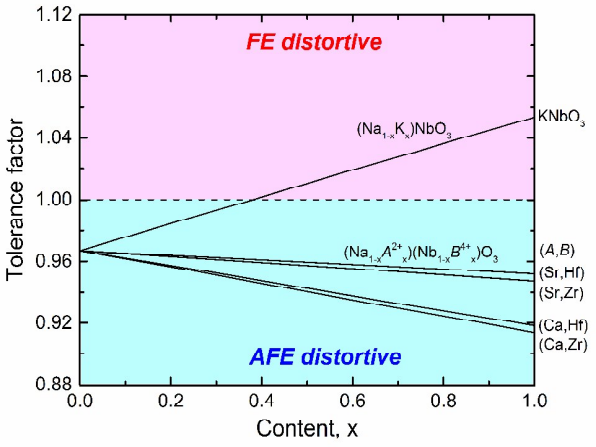

Fig. 1 Plot of average tolerance factor versus dopant concentration (x) to $NaNbO_3$. Red and blue part is ferroelectric and antiferroelectric distortive region respectively.

The rationalization of compositional trends and design of stable functional behaviour in perovskites can be assessed through the tolerance factor (t), electronegativity difference (X), and polarizability of the material. The Goldsmith tolerance factor t, is given by eq.(1), where R_A, R_B and R_O are ionic radii for the A- and B-cation sites and the oxygen anion.

$$t = (R_A + R_O)/2^{1/2}(R_B + R_O) \qquad (1)$$

The tolerance factors in this study were calculated using ionic radii from Shannon and Prewitt [30]. As shown in Fig. 1, the t factor can be generally categorized into two regions: AFE in blue and FE in red. Partial substitution of AFE cations, such as Zr^{4+} and Hf^{4+}, in the Nb site can decrease t and have a large effect on the polarizability of the system, enhancing AFE properties. In addition, partial substitution of divalent cations, such as Sr^{2+} and Ca^{2+}, in the Na site can lower t further and compensate for charge neutrality. In contrast, an increase of t factor is normally associated with an enhancement of polar distortions, such as in FE materials like $KNbO_3$ substituted NN. Halliyal and Shrout [31] found that a t versus average electronegativity diagram provided information on the stability of the perovskite family of compounds across different substitutions and solid solutions. The average electronegativity is expressed by

$$X = (X_{AO} + X_{BO})/2 \qquad (2)$$

where: X_{BO} is the electronegativity difference between the B cation and the oxygen anion, while X_{AO} is the electronegativity difference between the A cation and the oxygen anion. Figure 2 shows the relationship between t and X for various perovskite compounds, including a wide range of both simple and complex perovskites[31]. Complex lead perovskite compounds with both low t and X tend to favour the formation of pyrochlore phases, and the perovskite phase can be stabilized via solid solutions where either t or X are increased. It is interesting to note that many of the unstable complex compounds correspond to those that exhibit FE relaxor behaviour. AFEs, such as PZ and PIN, are positioned around $t = 0.964$. For NN, t is slightly larger than 0.964, as shown in both Figs. 1 and 2, and X is close to the value of $SrTiO_3$. We infer, therefore, that an AFE phase can be stabilized in NN by decreasing the value of t while keeping the value of X fixed.

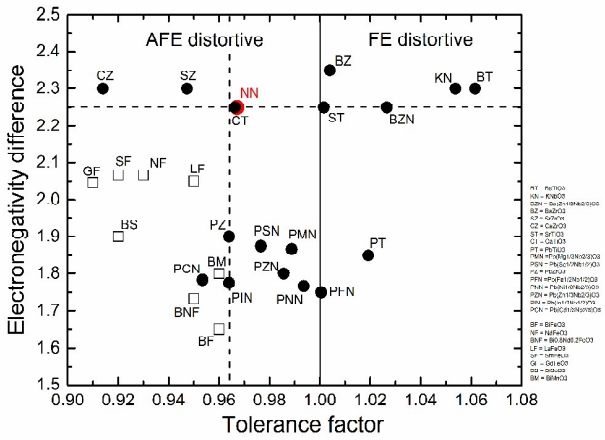

Fig. 2 Tolerance factor versus averaged electronegativity difference for various perovskites, where BT = $BaTiO_3$, KN = $KNbO_3$, BZN = $Ba(Zn_{1/3}Nb_{2/3})O_3$, BZ = $BaZrO_3$, SZ = $SrZrO_3$, CZ = $CaZrO_3$, ST = $SrTiO_3$, CT = $CaTiO_3$, PT = $PbTiO_3$, PMN = $Pb(Mg_{1/3}Nb_{2/3})O_3$, PSN = $Pb(Sc_{1/2}Nb_{1/2})O_3$, PZ = $PbZrO_3$, PFN = $Pb(Fe_{1/2}Nb_{1/2})O_3$, PNN = $Pb(Ni_{1/3}Nb_{2/3})O_3$, PZN = $Pb(Zn_{1/3}Nb_{2/3})O_3$, PIN = $Pb(In_{1/2}Nb_{1/2})O_3$, PCN = $Pb(Cd_{1/3}Nb_{2/3})O_3$, BF = $BiFeO_3$, NF = $NdFeO_3$, BNF = $Bi_{0.8}Nd_{0.2}FeO_3$, LF = $LaFeO_3$, SF = $SmFeO_3$, GF = $GdFeO_3$, BS = $BiScO_3$, BM = $BiMnO_3$

These observations are further supported by recent experimental results on $BiFeO_3$-based ceramics. Karimi *et al.* reported the appearance of a PZ-like AFE phase with Nd doping [32,33]. As the Nd-concentration increases, Nd-doped $BiFeO_3$ displayed double *P-E* loops. The transition from the *R3c* structure of $BiFeO_3$ to the PZ-like phase of $(Bi,Nd)FeO_3$ is attributed to a decrease in t. This decrease is small but more than sufficient to drive changes in symmetry; consider for instance the case of $Pb(Zr_{0.97}Ti_{0.03})O_3$ [34]. Similar diffraction patterns have been observed in rare-earth: Sm, Gd, and Dy doped $BiFeO_3$ based thin films [35]. In this case, solid solution doping provided a route for a transition from the FE rhombohedral phase of $BiFeO_3$ with *R3c* space group to an AFE structure with *Pnma* space group.

Figure 3 shows a more detailed relationship between t and X for $(Na_{1-x}A^{2+}{}_x)(Nb_{1-x}B^{4+}{}_x)O_3$ compositions, where (A,B) designates (Ca,Zr), (Ca,Hf), (Sr,Zr), and (Sr,Hf). The Ca-and Zr-substituted NN system: $(Na_{1-x}Ca_x)(Nb_{1-x}Zr_x)O_3$, shows the lowest t at a given substitution x for any $(Na_{1-x}A_x)(Nb_{1-x}B_x)O_3$ (A = Sr, Ca, and B = Hf, Zr) composition. From the viewpoint of the lowest t, the $(Na_{1-x}Ca_x)(Nb_{1-x}Zr_x)O_3$ ceramics (x = 0.00, 0.02, 0.04, 0.05, 0.06, and 0.10, abbreviated as CZNN100x hereafter or simply CZNN), were therefore, selected among these candidate combinations. The CZNN ceramics are expected to approach the same t as $PbZrO_3$ and a higher X than $SrTiO_3$. The end point member $CaZrO_3$ is a common dopant in a variety of FE perovskites. It has been known to improve the piezoelectric properties of FEs, such as in $(K_{0.5}Na_{0.5})NbO_3$- and

$BaTiO_3$-based systems [36, 37]. However, in the case of AFEs, especially for the lead-free compositions, its doping effect on the antiferroelectricity evolution has not yet been explored.

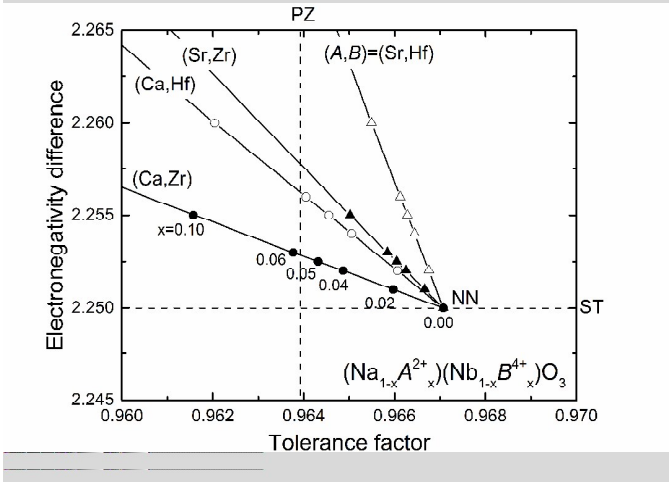

Fig. 3 Tolerance factor versus averaged electronegativity difference for $(Na_{1-x}A^{2+}_x)(Nb_{1-x}B^{4+}_x)O_3$ composition, where (A,B) = (Ca,Zr), (Ca,Hf), (Sr,Zr) and (Sr,Hf).

The materials designed strategy outlined earlier is applied to chemically stabilize antiferroelectricity in NN based ceramics. In this work, we perform X-ray diffraction and transmission electron microscopy structural analysis, as well as electrical measurements to study and describe the stabilization of antiferroelectricity in the CZNN system. Using first-principles calculations, we show that the AFE *P* phase of pure NN is stabilized in the CZNN ceramics due to the decrease of *t* in the system. Density functional total-energy and polarization calculations are used to rationalize the experimental observations and propose further investigations. The large decrease of polarization in the CZNN system is explained by a modification of the relative stability of the polar and nonpolar structures, effectively favouring nonpolar-to-polar AFE transitions over polar-to-polar FE domain switching.

2. Experimental Methods

CZNN ceramics were prepared by a conventional solid state method. The starting materials used in this study were reagent grade Na_2CO_3, $CaCO_3$, ZrO_2, and Nb_2O_5 (99.95%, 99.5%, 99.7%, and 99.9% purity, respectively; Alfa Aesar, Ward Hill, MA). The starting materials were dried at 200°C for 24 hours to remove absorbed water. These dried powders were then accurately weighed for each stoichiometric composition of CZNN and mixed with zirconia media and ethanol by ball milling for 24 h. The powders were calcined for 3 hours in a temperature range between 1000 and 1150°C in an air atmosphere. After each calcination, the powders were deflocculated and pressed into disk-shaped pellet without any binders; the pellets were then further pressed using cold isostatic pressing (CIP: Autoclave Engineers, Flow Autoclave Systems, Inc.). The pellets of calcined powders were sintered at 1320°C - 1400°C for 2 h in an air atmosphere. The crystal phases of the calcined powders and sintered ceramics were analyzed by powder X-ray diffraction (XRD, Model MRD; Panalytical, Almelo, The Netherlands) with CuKα radiation. Close-up examinations of the characteristic AFE superlattice peaks were followed by slow scanning. Dielectric and polarization measurements were performed on the densest sintered ceramics; these had been polished to 0.3 mm thickness with platinum electrodes deposited by a sputter coater (EMS150R S; Quorum).

Temperature dependences for dielectric constants and dielectric losses were measured at 1 kHz by LCR meter (4274A, Agilent Technologies Inc., Santa Clara, CA), with heating and cooling controlled conditions in an oven (DD-2300, Delta Design, Inc.). The *P-E* loops were measured using a modified Sawyer–Tower circuit with a frequency of 0.1 Hz and SIN waves at room temperature and 120°C.

Specimens for transmission electron microscopy (TEM) were prepared via standard procedures including grinding, cutting, dimpling, and ion milling. The dimpled disks were annealed at 400°C for 2h to minimize the residual stresses introduced during mechanical thinning. Then, the disks were further thinned with an Ar-ion mill until a perforation was formed. TEM studies were performed on a Philips EM420 microscopy operated at 120 kV.

3. Results and Discussions

3.1 AFE crystallography of $NaNbO_3$ - $CaZrO_3$ system

Numerous controversies surround the phase diagram of NN. The complex sequence of temperature - induced phase transitions has been studied by a number of researchers in a wide temperature range [18, 20, 27, 29, 38-43]. As mentioned earlier, Mishra *et al*. reported a coexistence of FE and AFE phases over a wide temperature range through neutron diffraction studies [29]. Anomalous smearing of the dielectric response of both phases over the same temperature range was consistent with coexistence and competition of FE and AFE interactions. Furthermore, Xu *et al*. recently reported that electric fields can induce an AFE phase out of a FE phase in NN-based lead-free polycrystalline ceramics [27]. According to their reports, the AFE phase consists of two or more sublattice dipole polarizations that are antiparallel, which in turn gives rise to a translational symmetry that creates superlattice reflections in the diffraction patterns. Figure 4 (a) shows XRD spectra for the CZNN ceramics. All the ceramics are phase pure with the perovskite structure and no remnant of ZrO_2 was recorded. Figure 4 (b) and (c) show respectively a close view of the XRD spectra around the {1 1 3/4} and {2 1 3/4} AFE superlattice peaks for the CZNN ceramics. These are the characteristic AFE superlattice peaks that can be indexed as {1 1 3/4} around 36.6° and {2 1 3/4} around 55.2°. The intensity of both superlattice peaks increased compared to NN ceramics and clearly decreased in CZNN10 ceramics. Although a solubility limitation could exist between CZNN6 and CZNN10, the observed trend implied that an AFE phase was stabilized.

For the case of NN, a complex physical behaviour has been found due to the variety of phases existing on a wide range of temperatures [44]. At room temperature, the AFE *P* phase (with space group *Pbma*) is commonly found [39,44-46]. Additionally, another polymorph of FE *Q* phase (with space group $P2_1ma$) is normally induced by a sufficient external electric field from *P* phase or by doping [45]. The *Q* phase can coexist with the *P* phase in virgin state single crystals [45,47,48], or appear in ceramic powders with reduced particle size to sub-micron scale [49,50], as well as in nanofilms [51-53].

Crystallographically, the primary difference between the *P* and *Q* phases derives from the off-center displacement of the B-site Nb ion, which combines with oxygen octahedral tilts around the *b*-axis direction of the pseudocubic unit cell [39,45].More specifically, the tilt system for the *Q* phase can be

denoted as $a^-b^+a^-$ in Glazer notation, while that for the *P* phase is described as a layered combination of $a^-b^+a^-$ and $a^-b^-a^-$ octahedral rotations [44,45]. Pairs of octahedral layers normal to [010] are related by a (010) mirror plane in the *Q* phase, inducing parallel Nb displacement arrays. The octahedral layers in the P phase are operated by a screw diad axis along [010], leading to an antiparallel displacement configuration [39,45]. Therefore, the unit cells of *Q* and *P* phases are, respectively, doubled and quadrupled in [010] direction [45]. Correspondingly, superlattice diffractions at 1/2{0*k*0}, for *Q* phase, and at 1/4{0*k*0}, for *P* phase, are expected in the reciprocal space [45].

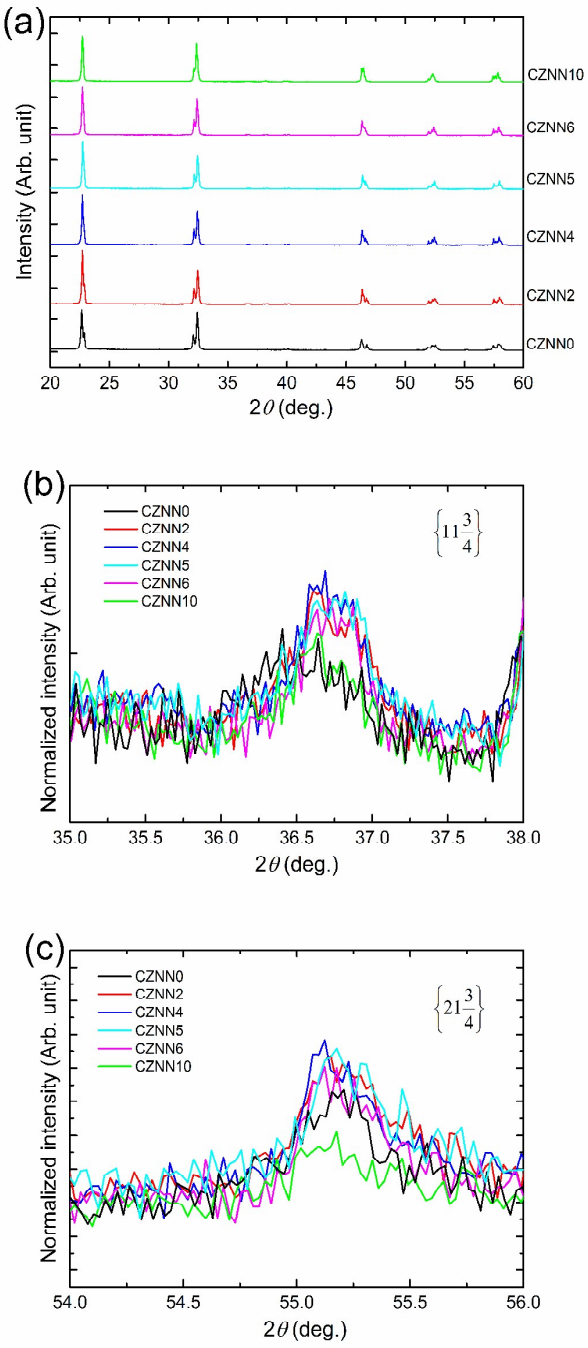

Fig. 4 (a) XRD spectra in the CZNN sintered ceramics. (b) Close view of XRD spectra around AFE {1 1 3/4} and (c) AFE {2 1 3/4} superlattice peaks in the CZNN sintered ceramics.

Based on the structural information discussed above, the domain morphology and crystal structure of as-sintered ceramics in the CZNN system were characterized by TEM, and the results are shown in Fig.5 for representative compositions. The [100] (or [001]) zone axis was mainly focused, especially for obtaining the electron diffraction patterns.

Representative grains in un-doped NN are displayed in Fig. 5a and 5d. The polydomain morphology composed of micron-sized domain blocks was manifested. The majority of the grains showed a single AFE *P* phase (Fig. 5a), as indicated by the quater-integral superlattice diffraction spots obtained from the selected area diffraction pattern for each domain (Fig. 5b and 5c). In addition, heterogeneity of un-doped NN is revealed with the presence of FE *Q* phase (domain area ② and ③ in Fig.5d), as manifested by the characteristic half-integral superlattice spots along [010] direction (Fig. 5f). Inside each domain blocks, translational domains with their well-defined walls parallel to [100] direction were observed for both *P* and *Q* phases, which is consistent with previous report [42].

Further verification of these translational domain walls, instead of orientational domain walls, was performed by careful diffraction analysis. No spots splitting, either the fundamental or the superlattice reflections, was observed for *P* and *Q* phases, suggesting that these translational domain walls cannot be ferroelastic twin boundaries [45]. Instead, the translational domain walls in FE *Q* phase were determined as mixed inversion-translation type, where the adjacent two domains forming the translational domain wall have the same orientational state but inversion related [45]. In addition to the translational domain walls, orientational domain walls were imaged, as exemplified by the short arrows combined with the domain wall types. It has been known that two types of AFE domain walls (AFD), namely 90° AFD and 60° AFD, are permissible in the *P* phase NN under an uncharged configuration [45]. The habit planes were determined as {100} for 90° AFD, and {110} for 60° AFD [45], while for the FE *Q* phase in the present study (Fig.5d), the {100} plane is assigned as 90° FE domain wall (FD) [45]. With CZ substitution, a similar feature was maintained for the polydomain morphology, as displayed by the representative grains in Fig.5g for CZNN4 and Fig.5j for CZNN5. However, all the <100> zone axes diffraction pattern for each domain region showed the characteristic quartering along [010] direction (Fig.5h, 5i, 5k, and 5l), suggesting the AFE *P* type for the phase structure.

Furthermore, the possibility of the presence of FE *Q* phase in the doped compositions are most likely ruled out, based on the fact that the 1/2{010}-type superlattice diffractions (i.e. Fig.5f) were not found in an extensive TEM examination on about 15 grains for each doped composition. Therefore, the TEM results are in good correspondence with the *P-E* measurements (shown in section 3.3); in pure NN, the coexistence of AFE *P* phase and FE *Q* phase suggests a comparative free-energy profile between them, with the latter one as a metastable state. With the increase of substitution content to 4%, or 5%, the AFE phase is further favoured and stabilized at the expenses of FE phase, which contributes to the presence of double *P-E* loops for the corresponding compositions.

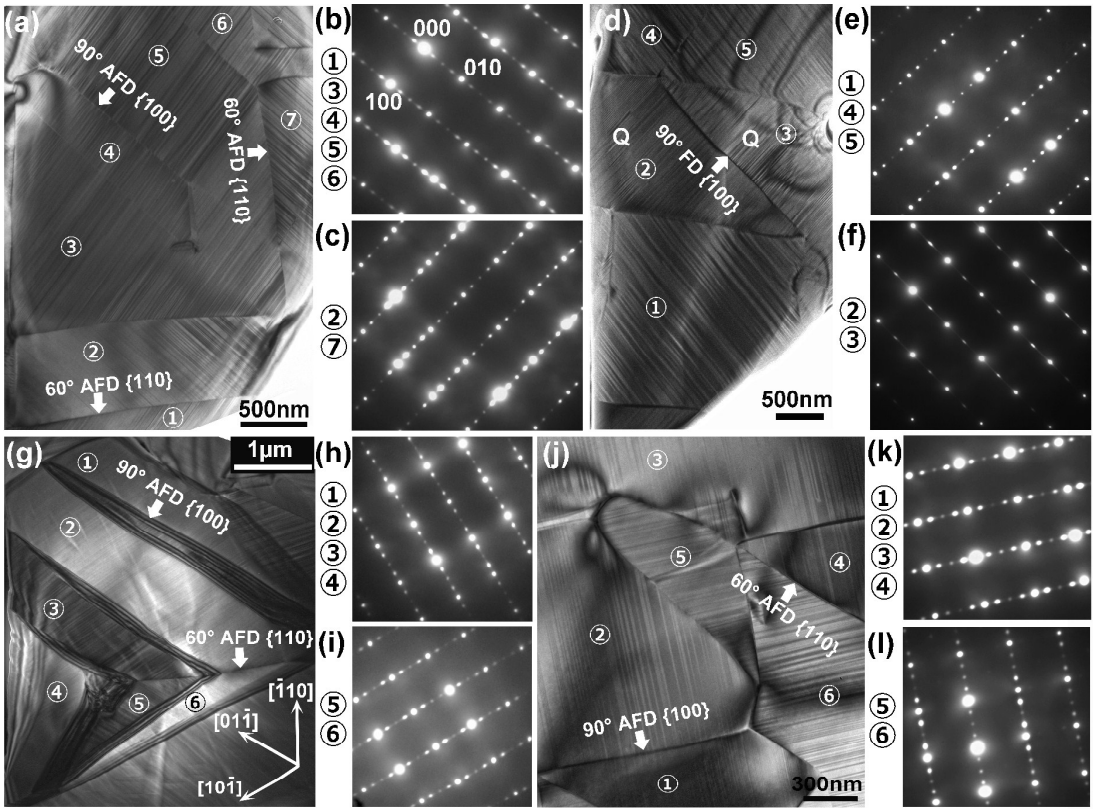

Fig. 5 Characterization of the domain morphology and crystal structures in CZNN100*x* (*x* = 0.00, 0.04 and 0.05) ceramics for representative grains. Bright field image for a (a) [100]-aligned grain in CZNN0 with pure AFE P phase; (d) [100]-aligned grain in CZNN0 with the coexistence of AFE P phase and FE Q phase; (g) [111]-aligned grain in CZNN4; and (j) [100]-aligned grain in CZNN5. Each domain area is numerically marked. The [100] zone axis diffraction patterns from each single domain are shown as (b) and (c) for CZNN0, (h) and (i) for CZNN4, and (k) and (l) for CZNN5, with P phase only; and (e) and (f) for CZNN0 with the coexistence of P and Q phases. The bright field images shown in (a), (d), (g) and (j) are recorded several degree off the zone axis in order to show the contrast of the translational domains. The characteristic orientational domain walls are marked by the bright short arrows. Here AFE and FE domain walls are referred shortly as AFD and FD, respectively.

3.2 The dielectric behaviour and phase transition in high temperature

Figure 6 (a) and (b) show, respectively, the dielectric permittivity and dielectric loss of CZNN ceramics as a function of temperature. These measurements were realized at 1 kHz on both heating and cooling processes, at a rate of 2°C/min. The first order AFE - FE transition has thermal hysteresis for all the compositions considered in this work. In NN ceramics, there is a clear dielectric peak around 350°C, typically attributed to the AFE structural phase transition from the orthorhombic *R* phase with *Pmnm* space group to the orthorhombic *P* phase with *Pbma* structure. This phase transition temperature is identified as T_C [18, 38, 54].

As shown in Fig. 6 (a), the T_C of CZNN ceramic is shifted to lower temperatures with increasing *x*, and the dielectric constant around T_C is also decreased and turned over between CZNN5 and CZNN6. As shown in Fig. 6 (b), the CZNN ceramics showed smaller dielectric loss at high temperatures compared to NN ceramics, which presumably include more sodium and oxygen vacancy resulting from air sintering process. It is likely that the Ca-and Zr-substitution can make the polarizability of the system decrease, as expected from the *t*.

The thermal hysteresis and the magnitude of the thermal hysteresis, as well as the enthalpy of the phase transition, are all sensitive to dopants and defect concentrations [55]. Figure 6 (c) shows thermal hysteresis gap, $\Delta T/T_{cooling}$, as a function of *x*. The temperature gap ΔT between thermal hysteresis in heating and cooling was divided by $T_{cooling}$ and plotted versus *x*. The $\Delta T/T_{cooling}$ of the CZNN2 ceramic was almost same as that of the NN ceramic, and the $\Delta T/T_{cooling}$ gradually increased from CZNN2 up to CZNN6.

3.3 Electric field-induced AFE - FE phase transition

P-E loops of CZNN ceramics were measured at room temperature and at 120 °C. At room temperature, NN ceramics showed typical square-shaped *P-E* loop, as previously reported [26]. Therefore, the evidence of AFE superlattice structure in the mixed *P*/*Q* phases implies a limit in measurement resolution for the back switching to the AFE *P* phase. The CZNN2 ceramic showed double hysteresis loops, even though is still clamped at room temperature. The CZNN4 and CZNN5 ceramics did not show clear double hysteresis loops because of their high coercive fields. In the measurements at 120 °C, the Ca-and Zr-substituted CZNN ceramics showed clear double hysteresis loops, as shown in Figure 7 (a). It should be noted that the signature double hysteresis loops were not obtained for CZNN6 and CZNN10 ceramics. In the former case, the double P-E loop

was not achievable before the breakdown, indicating that the AFE-to-FE switching field E_F is higher than the breakdown strength; while for CZNN10 ceramics, it is out of the solubility limitation range since our TEM study suggests an incompatible microstructure and diffraction behaviour with other compositions with $x \leq 0.05$.

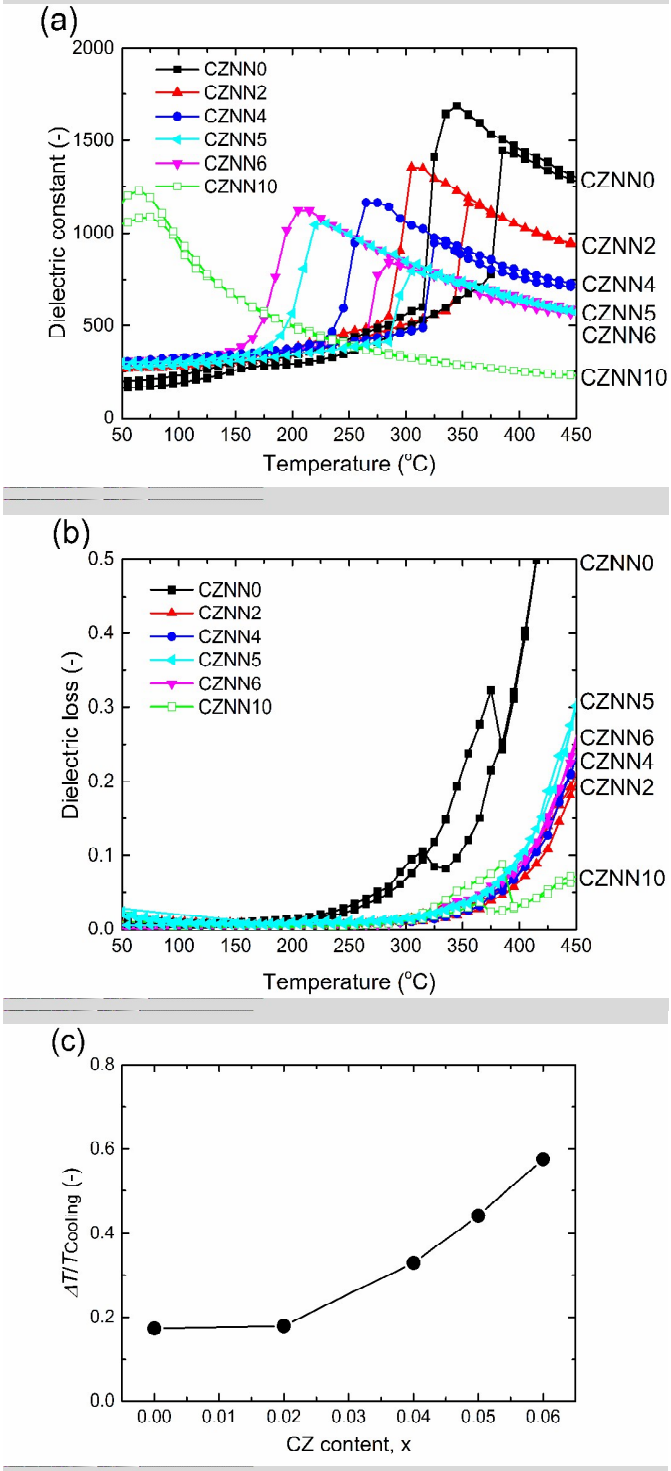

Fig. 6 The temperature dependences of (a) dielectric constant and (b) dielectric loss in CZNN ceramics. They were measured at 1 kHz in both heating and cooling process. (c) Relation of ΔT (= $T_{heating}$ - $T_{cooling}$) / $T_{cooling}$ and Ca-and Zr-substitution amount.

As mentioned above, the NN ceramic showed a square *P-E* loop resulting from a field-induced metastable FE. In contrast, the CZNN2, CZNN4, and CZNN5 ceramics showed typical double *P-E* loops, corroborating the enhancement of AFE superlattice peaks. Figure 7 (b) shows the relation between the maximum field-induced polarization (P_{max}) and the E_F as a function of substitution *x*.

The differential dielectric constants (ε_d) in the CZNN ceramics were obtained by differentiating the P_{max}. The P_{max} and the ε_d in the CZNN ceramics decreased corresponding to dielectric constants behaviour shown in Fig. 6 (a). The E_F was increased from 0 to 150 kV/cm with 6% substitution. This means that (Ca,Zr) substitution leads to wide range of antiferroelectricity, with coercive fields up to 150 kV/cm. These results are similar to previous investigations in traditional FE, such as $BiFeO_3$. Finally, electrical *P* vs. *t* data, and the field dependency of dielectric permittivity is also consistent with AFE and the permittivity increase at the E_F. This is ultimately an important practical characteristic for high voltage capacitor applications.

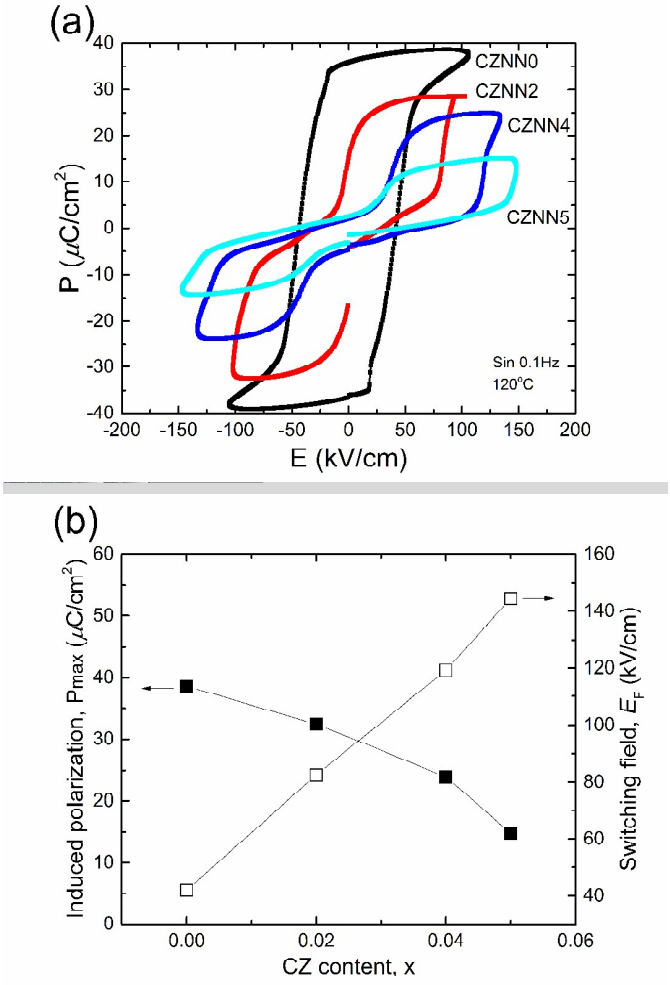

Fig. 7 (a) *P-E* loops in the CZNN ceramics at high temperature of 120 °C, (b) the relation of induced polarization and switching field ($E_{AFE\ to\ FE}$) and *x*.

3.4 First principles calculations

In order to obtain further insights into the competition and coexistence of antiferroelectricity and ferroelectricity in

NN based ceramics, we have performed first principles calculations to explore the structural and electronic properties of the relevant structural phases. In this section, we focus on experimentally reported phases of pure NN at room and low temperatures. As we will show later, the effect of (Ca,Zr) doping in the CZNN system can be modelled as a small perturbation of pure NN.

Density functional calculations were performed using version 7.8.2 of the ABINIT package [56]. Accurate total-energy calculations [57] were obtained with the generalized gradient approximation (GGA) [58] and PAW pseudopotentials [59]. The electronic contribution to the total polarization is obtained using the modern theory of polarization [60], as implemented in ABINIT.

The relative energy difference of the relevant structures (the high-symmetry cubic reference $Pm\bar{3}m$ phase, the $P2_1ma$ (Q) phase, the $Pbma$ (P) phase, and the low-temperature $R3c$ phase) are reported in Table I. For each structure considered, we optimized the lattice parameters as a bulk phase and calculate the volume and total polarization. Experimental lattice parameters [61-63] are overestimated by 1%, typical for GGA. We find that the $R3c$ structure is lowest in energy, in agreement with experiments. The structure of $R3c$ is obtained by the simultaneous combination of the polar mode along 111 and a $c^-c^-c^-$ octahedral rotation

We find a remarkably small energy difference between the nonpolar $Pbma$ and polar $P2_1ma$ structures, on the order of 1 meV, which is a key characteristic of antiferroelectricity [64,65]. The small energy difference between these phases can be attributed to the structural similarities mentioned in section 3.1, while these two structures differ considerably from the $R3c$ structure. Assuming that the critical field E_c required to overcome the AFE energy barrier is given by $E_c \sim \Delta E/V_cP_c$, with P_c and V_c the polarization and volume of the $P2_1ma$ phase given in Table I, we estimate the E_F as 150 kV/cm.

The experimental value for the polarization of NN is smaller than the calculated polarizations for $P2_1ma$ and $R3c$. However, if we take into account that the experimental measurement is on a polycrystalline sample and the first-principles value is for a single crystal, we should compare the experimental value to a poled random orientation average, which should reduce the polarization (an approximate calculation yields a factor of 5/6), making the experimental value very close to that predicted from first principles.

Table I: Energy ΔE (meV/5atoms), volume expansion $\Delta V/V$ (%), lattice parameters (Latt.) in Å (β is the angle in the rhombohedral cell), and total polarization P (μC/cm^2) for the experimental phases of NN.

Phase	ΔE	$\Delta V/V$	Latt. (Å)			P
$Pm\bar{3}m$	0	0	3.974			0
$P2_1ma$	-108.7	-1.86	5.59	5.65	7.79	47
$Pbma$	-106.3	-2.48	5.56	5.64	15.59	0
$R3c$	-116.1	-1.67	5.63	β = 58.97°		58

The task is now to rationalize the experimental results of section 3.3 using the first principles calculations. Substitution of (Ca,Zr) in NN has a large effect on the CZNN system. There is a clear crossover from ferroelectricity to antiferroelectricity under a small (Ca,Zr) substitution. Double hysteresis loops are observed between 2% and 6% (Ca,Zr) substitution, implying a small energy difference between $Pbma$ and $P2_1ma$ in this entire composition range. At ~6%, the field-induced polarization has decreased by 60% (from ~40 to ~15 μC/cm^2) and the AFE critical field E_F has tripled (from ~50 to ~150 kV/cm).

We suggest a two-fold interpretation of these changes, the first reflecting the changes in energetics of the relevant phases with substitution, and the second having to do with the polycrystalline nature of the samples.

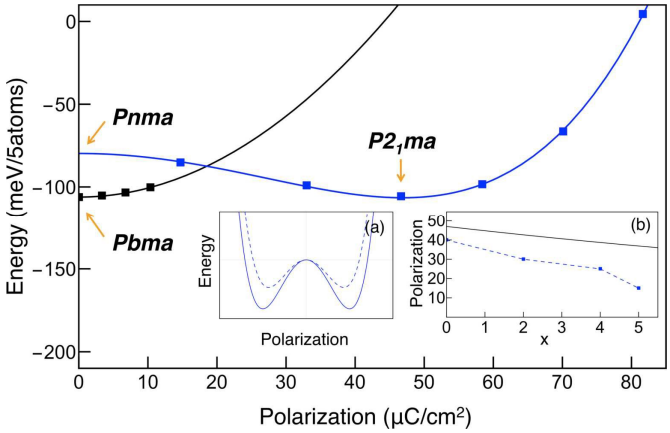

Fig. 8 First principles calculation of the energy as a function of polarization for the $Pbma$ and $P2_1ma$ structures. Insets: (a) Schematic representation of the effect of lowering the tolerance factor in the stability of the FE phase. (b) Experimental (dash line) and estimated (solid line) magnitude for the field-induced polarization as a function of doping.

First, in Figure 8 we show the energies of the two phases as a function of polarization; these curves are obtained by constraining the amplitude of a polar distortion, relaxing all other structural parameters, and then extracting the resulting polarization and total energy. The main changes expected with substitution x are a decrease in the energy of the nonpolar $Pnma$ phase relative to the nonpolar $Pbma$ phase, and a decrease in the magnitude of the negative curvature of the double well. The first can be associated with the eventual transition to the $Pnma$ structure of the endpoint compound $CaZrO_3$ with increasing x. The second can be associated with the decrease in the tolerance factor, which tends to reduce the strength of the FE instability; this will reduce the polarization of the minimum energy $P2_1ma$ structure, as shown in Fig. 8 (a). These two changes should be related so as to favour the nonpolar $Pbma$ phase with increasing x, while keeping the energy difference between the nonpolar $Pbma$ phase and the polar $P2_1ma$ phase within a few meV, consistent with the observed critical fields E_F.

The stabilization of the AFE behaviour and the strong dependence on x of the polarization is expected to have a second contribution associated with the polycrystalline nature of the system, resulting from an increase in the energy difference between the nonpolar P phase and the polar Q phase. To see this, we assume that the system can be separated into nonpolar (n_{np}) and polar (n_p) domains. The latter can be subsequently divided among those domains that switch between polar states (n_{FE}) and those that switch between nonpolar and polar states (n_{AFE}). Given that, in this case, the FE phase that coexists with $Pbma$ corresponds also to the field-induced FE phase, n_{FE} and n_{AFE} have the same field-induced polarization. Therefore, the total polarization of the system (as a function of doping x and field E) can be approximated as:

$$P = P_0\, n_p,$$

where P_0 is the polarization of the polar $P2_1ma$ phase and n_p is the volumetric density of polar domains. The density of polar domains can be approximated by the probability of switching to the polar (rather than the nonpolar) state, which is given by the Boltzmann distribution $e^{-E/kT}$ of n_{FE} and $n_{AFE,}$ where T is the temperature, k is Boltzmann constant, and E is the total energy for the $Pbma$ and $P2_1ma$ structures. Assuming that the energy difference between $Pbma$ and $P2_1ma$ varies linearly as a function of the doping x, and is roughly zero at x = 0% and on the order of 10 meV at x = 6% doping, we obtain:

$$P = P_0\, n_p = P_0\, e^{-\Delta E/kT} = P_0\, e^{-E0x/kT}$$

with E_0 = 4.8 meV, P_0 = 47 μC/cm^2 and kT = 34 meV for the CZNN system. As shown in Fig. 8 (b), we find that this simple model is capable of reproducing the qualitative behaviour of the macroscopic field-induced polarization.

The hysteresis behaviour of the CZNN system is, therefore, explained by the modification of the relative stability of the competing nonpolar and polar structures and thermodynamic effects on the system. In pure NN, the energy difference between $Pbma$ and $P2_1ma$ is essentially zero, and the metastable FE phase is stabilized under a small external field required to overcome the energy barrier between these structures. We speculate that, while the majority of the domains undergo polar-to-polar FE switching at x = 0, surrounding the potential minimum at $Pbma$, the FE hysteresis behaviour is suppressed by the increase of energy difference between $P2_1ma$ and the ground state $Pbma$. The number of domains that switch from polar to polar decreases, increasing the number of domains switching between the polar and nonpolar phase, leading to a decrease of macroscopic polarization.

Further knowledge of the energy landscape between the structures would provide further information on the role of kinetic in the AFE transition. As mentioned earlier, the rather slow kinetic of the AFE switching competes with FE domain transitions in NN based ceramics. During a continuous cycling of the applied field, the FE state is largely suppressed by an increase of the AFE energy barrier, which must also be overcome during a macroscopic polar-to-polar FE switching path.

Conclusions

In this work we demonstrated the stabilization of antiferroelectricity in $NaNbO_3$ based ceramics under partial substitution of Ca^{2+} and Zr^{4+} in $NaNbO_3$. The polarizability and electronegativity of the solid solution $(Na,Ca)(Nb,Zr)O_3$ are modified by the decreases in tolerance factor, effectively favouring the stabilization of antiferroelectricity over ferroelectricity.

The appearance of antiferroelectricity is confirmed through superlattice reflections, dielectric measurements, XRD studies of domain structures, and P-E hysteresis measurements. The large increase in the AFE-to-FE switching field and decrease of field-induced polarization were rationalized using first principles calculations. The relative energy difference between the nonpolar and polar structures was modified, effectively increasing the probability of switching to the nonpolar state. We hope that this work will motivate the design of more lead-free AFE dielectrics and provide new opportunities for lead-free AFE capacitor applications.

Acknowledgements

Hiroyuki Shimizu gratefully acknowledges technical assistance from Jeff Long, Steven Perini, Rudeger H. T. Wilkes and Amanda Baker at The Pennsylvania State University, and also wishes to thank Taiyo Yuden Corporation - Visiting Scientist Grant. S. E. Reyes-Lillo would like to thank Susan Trolier-McKinstry for useful conversations and her hospitality at the Materials Research Institute of the Pennsylvania State University.

Notes and references

[a] Taiyo Yuden Co., Ltd., Takasaki, Gunma 370-3347, Japan
[b] Center for Dielectrics and Piezoelectrics, Materials Research Institute, The Pennsylvania State University, University Park, PA 16802, USA
[c] Department of Physics and Astronomy, Rutgers University, Piscataway, NJ 08854-8019

1 J. P. Dougherty, United States Patent 5, 1996, **184**, 545.
2. Z. Xu, X. Dai, D. Viehland, and D. A. Payne, *J. Am. Ceram. Soc.*, 1995, **78**, 2220.
3. T. Asada and Y. Koyama, *Phys. Rev. B*, 2004, **69**, 104108.
4. E. Sawaguchi, H. Maniwa, and S. Hoshino, *Phys. Rev.*, 1951, **83**, 1078.
5. G. Shirane, E. Sawaguchi, and Y. Takagi, *Phys. Rev.*, 1951, **84**, 476–81.
6. G. Shirane and R. Pepinsky, *Phys. Rev.*, 1953, **91**, 812–5.
7. G. A. Samara, *Phys. Rev. B*, 1970, **1**, 3777–86.
8. C. A. Randall, D. J. Barber, P. Groves, R. W. Whatmore, *J. Mat. Sci.*, 1988, **23**, 3678-82.
9. Z. Xu, D. Viehland, P. Yang, and D. A. Payne, *J. Appl. Phys.*, 1993, **74**, 3406.
10. Z. Xu, D. Viehland, and D. A. Payne, *J. Mater. Res.*, 1995, **10**, 4538.
11. Y. Gai, F. Phillipp, A. Zimmermann, L. Zhou, F. Aldinger, and M. Ruhle, *Acta Mater.*, 2003, **51**, 6429.
12. H. He and X. Tan, *Phys. Rev. B*, 2005, **72**, 024102.
13. X. Tan, J. Frederick, C. Ma, W. Jo, and J. Rödel, *Phys. Rev. Lett.*, 2010, **105**, 255702.
14. K. Uchino and M. Aizawa, *Jpn. J. Appl. Phys.*, 1985, **24**, 139.
15. W. Pan, Q. Zhang, A. Bhalla, and L. E. Cross, *J. Am. Ceram. Soc.*, 1989, **72**, 571.
16. Y. Saito, H. Takao, T. Tani, T. Nonoyama, K. Takatori, T. Homma, T. Nagaya, and M. Nakamura, Nature, 2004, **432**, 84–7.
17. J. Rödel, W. Jo, K. Seifert, E. M. Anton, T. Granzow, and D. Damjanovic, *J. Am. Ceram. Soc.*, 2009, **92**, 1153–77.
18. X. Tan, C. Ma, J. Frederick, S. Beckman, and K. G. Webber, *J. Am. Ceram. Soc.*, 2011, **94** [12], 4091–4107.
19. E. A. Wood, R. C. Miller, and J. P. Remeika, *Acta Cryst.*, 1962, **15**, 1273–9.
20. I. Lefkowitz, K. Lukaszewicz, and H. D. Megaw, *Acta Cryst.*, 1966, **20**, 670–83.
21. R. H. Dungan and R. D. Golding, *J. Amer. Ceram. Soc.*, 1964, **47** [2], 73–76.
22. A. V. Ulinzheyev, O. E. Fesenko, and V. G. Smotrakov, *Ferroelec. Lett.*, 1990, **12** [1], 17–21.
23. A. V. Ulinzheev, A. V. Leiderman, V. G. Smotrakov, V. Yu. Topolov, and O. E. Fesenko, *Phys. Solid State*, 1997, **39** [6], 972–4.
24. V. A. Shuvaeva, M. Yu. Antipin, R. S. V. Lindeman, O. E. Fesenko, V. G. Smotrakov, and Yu. T. Struchkov, *Ferroelect.*, 1993, **141**[1], 307–31.
25. T. Arioka, H. Taniguchi, M. Itoh, K. Oka, R. Wang, and D. Fu, *Ferroelect.*, 2010, **401**, 51–5.
26. H. Shimizu, K. Kobayashi, Y. Mizuno, and C. A. Randall, *J. Am. Ceram. Soc.*, 2014, **97** [6], 1791-1796.
27. Y. Xu, W. Hong, Y. Feng, and X. Tan, *Appl. Phys. Lett.*, 2014, **104**, 052903.
28. D. Fu, T. Arioka, H. Taniguchi, T. Taniyama, and M. Itoh, *Appl. Phys. Lett.*, 2011, **99**, 012904.
29. S. K. Mishra, N. Choudhury, S. L. Chaplot, P. S. R. Krishna, and R. Mittal, *Phys. Rev. B.*, 2007, **76**, 024110.
30. R. D. Shannon and C.T. Prewitt, *Acta Cryst.*, 1969, **B25**, 925.

31. A. Halliyal and T. R. Shrout, *Am. Ceram. Conf.* (Regional), New Orleans, 1986.
32. S. Karimi, I. M. Reaney, Y. Han, J. Pokorny, I. Sterianou, *J Mater Sci*, 2009, **44**, 5102–5112.
33. S. Karimi, I. M. Reaney, I. Levin, and I. Sterianou, *Appl. Phys. Lett.*, 2009, **94**, 112903.
34. D. I. Woodward, J. Knudsen, and I. M. Reaney, *Phys. Rev. B*, 2005, **72**, 104110.
35. D. Kan, L. Palova, V. Anbusathaiah, C. J. Cheng, S. Fujino, V. Nagarajan, K. M. Rabe and I. Takeuchi, *Adv. Funct. Mater.*, 2010, **20**, 1108.
36. W. Liang, W. Wu, D. Xiao, and J. Zhu, *J. Am. Ceram. Soc.*, 2011, **94**, 4317-22.
37. W. Liu and X. Ren, *Phys. Rev. Lett.*, 2009, **103**, 257602.
38. S. K. Mishra, R. Mittal, V. Yu. Pomjakushin, and S. L. Chaplot, *Phys. Rev. B.*, 2011, **83**, 134105.
39. A. C. Sakowishi-Cowley, K. Lokaszewicz, and H.D. Megaw, *Acta Cryst.*, 1969, **B25**, 851-65.
40. A. M. Glazer and H. D. Megaw, *Philos. Mag.*, 1972, **25**, 1119–35.
41. M. Ahtee, A. M. Glazer, and H. D. Megaw, *Philos. Mag.*, 1972, **26**, 995–1014.
42. C. N. W. Darlington and H. D. Megaw, *Acta Crystallogr.*, 1973, **29**, 2171–85.
43. Yu. I. Yuzyuk, P. Simon, E. Gagarina, L. Hennet, D. Thiaudiere, V. I. Torgashev, S. I. Raevskya, I. P. Raevskii, L. A. Reznitchenko, and J. L. Sauvajol, *J. Phys. Condens. Matter.*, 2005, **17**, 4977–90.
44. A. M. Glazer and H.D. Megaw, *Acta Cryst.*, 1973, **A29**, 489.
45. J. Chen and D. Feng, *Phys. Stat. Sol. (a)*, 1988, **109**, 171.
46. H. D. Megaw and M. Wells, *Acta Cryst.*, 1958, **11**, 858.
47. R. A. Shakhovoy, S. I. Raevskaya, L. A. Shakhovaya, D. V. Suzdalev, I. P. Raevski, Y. I. Yuzyuk, A. F. Semenchev, and M. E. Marssi, *J. Raman Spectrosc.*, 2012, **43**, 1141.
48. L. A. Reznichenko, L. A. Shikina, E. S. Gagarina, I. P. Raevkiĭ, E. A. Dul'kin, E. M. Kuznetsova, and V. V. Akhnazarova, *Crystallogr. Rep.*, 2003, **48**, 448.
49. Y. Shiratori, A. Magrez, W. Fischer, C. Pithan, and R. Waser, *J. Phys. Chem. C*, 2007, **111**, 18493.
50. J. Koruza, J. Tellier, B. Malič, V. Bobnar, and M. Kosec, *J. Appl. Phys.*, 2010, **108**, 113509.
51. M. Tyunina and J. Levoska, *Appl. Phys. Lett.*, 2009, **95**, 102903.
52. S. Yamazoe, A. Kohori, H. Sakurai, Y. Kitanaka, Y. Noguchi, M. miyayama, and T. Wada, *J. Appl. Phys.*, 2012, **112**, 052007.
53. Y. I. Yuzyuk, R. A. Shakhovoy, S. I. Raevskaya, I. P. Raevski, M. E. Marssi, M. G. Karkut, and P. Simon, *Appl. Phys. Lett.*, 2010, **96**, 222904.
54. L. A. Reznitchenko, A. V. Turik, E. M. Kuznetsova, and V. P. Sakhnenko, *J. Phys.: Condens. Matter*., 2001, **13[17]**, 3875–81.
55. A. P. Levanyuk, S. A. Minyukov, and M. Vallade, *J. Phys.: Condens. Matter.*, 1997, **9[25]**, 5313–20.
56. X. Gonze, B. Amadon, P. Anglade, J. M. Beuken, F. Bottin, P. Boulanger, F. Bruneval, D. Caliste, R. Caracas, M. Cote, *Comput. Phys. Commun.*, 2009, **180**, 2582.
57. We note that the local density approximation (LDA) combined with PAW pseudopotentials is not able to correctly predict the energy ordering between the structures.
58. J. P. Perdew, K. Burke, M. Ernzerhof, *Phys Rev Lett.*, 1996, **77**, 3865.
59. G. Kresse and D. Joubert, *Phys Rev B*, 1999, **59**, 1758.
60. R. D. King-Smith and D. Vanderbilt, *Phys. Rev. B*, 1993, **47**, R1651.
61. S. P. Solovev, Y. N. Venevtsev and G. S. Zhdanov Sov. *Phys. Cryst*., 1961, **6**, 218.
62. K. E. Johnston, C. C. Tang, J. E. Parker, K. S. Knight, P. Lightfoot and S. E. Ashbrook, *J. Am. Chem. Soc.,* 2010, **132**, 8732.
63. C. N. W. Darlington, H. D. Megaw, *Acta Cryst.*, 1973, **B29**, 2171.
64. K. M. Rabe, in Functional Metal Oxides: New Science and Novel Applications, ed. by Satish Ogale and V. Venkateshan, Wiley (2013).
65. S. E. Reyes-Lillo and K. M. Rabe, *Phys. Rev. B*, 2013, **88**, 180102(R).

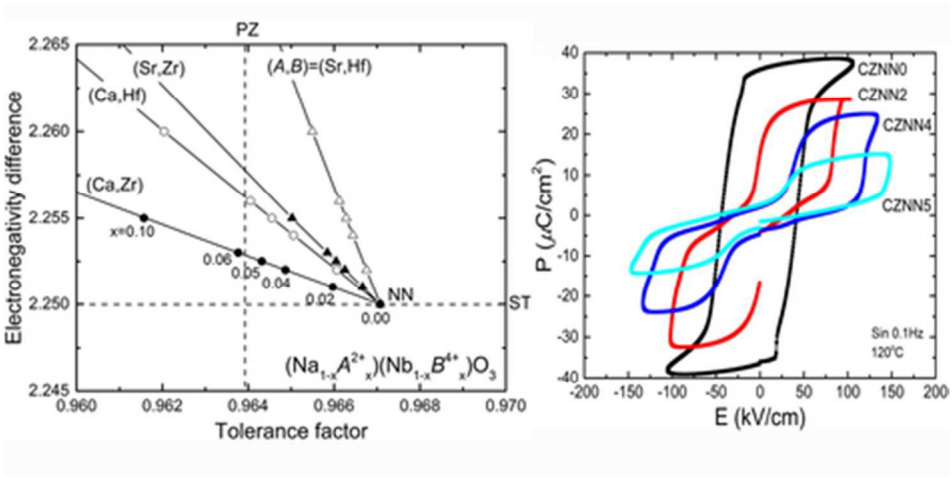

Crystal chemistry modification stabilized antiferroelectricity in $NaNbO_3$-based polycrystalline ceramics.
39x19mm (300 x 300 DPI)